In-flight degradation correction of SCIAMACHY UV reflectances and Absorbing Aerosol Index

L. G. Tilstra,[1] M. de Graaf,[1] I. Aben,[2] and P. Stammes[1]

[1]   In this paper we study the close relationship between the radiometric calibration of a satellite instrument and the Absorbing Aerosol Index (AAI) derived from the observed Earth reflectance. Instrument degradation of the Scanning Imaging Absorption Spectrometer for Atmospheric Chartography (SCIAMACHY) instrument in the ultraviolet wavelength range is examined by analyzing time series of global means of the AAI, making use of the experience that the global mean should be more or less constant when instrument degradation is absent. The analysis reveals the magnitude of the (scan angle dependent) instrument degradation of SCIAMACHY and also shows that currently available correction techniques are not able to correct the instrument degradation in a sufficient manner. We therefore develop and introduce a new method for degradation correction, which is based on the analysis of the time evolution of the global mean reflectance. Seasonal variations in the global mean reflectance, which mainly result from seasonal variations in scattering geometry and global cloud coverage, are separated from the time series in order to isolate the instrument degradation. Finally, we apply the derived reflectance correction factors to the SCIAMACHY reflectances and calculate the AAI to find that the effects of instrument degradation are reduced to within the 0.1 index point level. The derived AAI is also compared with the AAI based on other correction techniques. The proposed in-flight reflectance degradation correction method performs best in all aspects.

Citation: Tilstra, L. G., M. de Graaf, I. Aben, and P. Stammes (2012), In-flight degradation correction of SCIAMACHY UV reflectances and Absorbing Aerosol Index, *J. Geophys. Res.*, *117*, D06209, doi:10.1029/2011JD016957.

1. Introduction

[2]   The Absorbing Aerosol Index (AAI) was originally developed to support the Total Ozone Mapping Spectrometer (TOMS) ozone retrieval algorithm [*Herman et al.*, 1997; *Torres et al.*, 1998]. The AAI is a unitless index, capable of detecting UV-absorbing aerosols over land and water surfaces, even in the presence of clouds when the aerosol layer overlies the clouds [*Torres et al.*, 1998; *de Graaf et al.*, 2005]. As a result, it is a commonly used tool for aerosol screening. Other uses include the detection of smoke from forest fires and the monitoring of ash from volcanic eruptions. The AAI products from several remote sensing satellite instruments provide support to Volcanic Ash Advisory Centers (VAAC, see, for instance, http://www.metoffice.gov.uk/aviation/vaac/). Because of the long data record that is available (TOMS measurements started in 1978), the TOMS AAI is also used for studies into the impact of aerosols on climate. The AAI algorithm is robust and relatively easy to implement.

[3]   Unfortunately, the AAI is also very sensitive to the effects of instrument degradation, as will be shown in this paper. Satellite instruments like Global Ozone Monitoring Experiment (GOME) [*Burrows et al.* [1999], Scanning Imaging Absorption Spectrometer for Atmospheric Chartography (SCIAMACHY) [*Bovensmann et al.* [1999], and GOME-2 [*Callies et al.*, 2000] are subject to strong instrument degradation in the ultraviolet (UV) wavelength range, from which the AAI is determined. An exception is the Ozone Monitoring Instrument (OMI) [*Levelt et al.*, 2006], which shows little or no degradation probably owing to its completely different instrument concept. In this paper, we will focus on the AAI determined from SCIAMACHY measurements. A proper and accurate handling of instrument degradation is in this case essential.

[4]   The radiometric calibration of SCIAMACHY has received much attention in the past. Many efforts were made to study and improve the radiometric calibration using satellite intercomparisons [*Acarreta and Stammes*, 2005; *Noël et al.*, 2007a; *von Hoyningen-Huene et al.*, 2007; *Kokhanovsky et al.*, 2007; *Tilstra and Stammes*, 2006, 2007; *Jourdan et al.*, 2007] and comparisons with radiative transfer calculations [*van Soest et al.*, 2005;

---

[1]Climate Research and Seismology Department, Royal Netherlands Meteorological Institute, De Bilt, Netherlands.
[2]Division of Earth and Planetary Science, Netherlands Institute for Space Research, Utrecht, Netherlands.

Tilstra et al., 2005]. These studies were all based on data from up to a few years after launch, for which instrument degradation is not such an issue, or they were focused on wavelengths outside the UV wavelength range, where the impact of instrument degradation is small. Few dedicated publications on SCIAMACHY instrument degradation [*Noël et al.*, 2007b; *Bramstedt et al.*, 2009] and its impact on level 1 and derived level 2 products have appeared. This paper is meant to fill that gap, since the level 1 product is the basis for many other products.

[5] The goal of this paper is threefold: (1) to show that the sensitivity of the AAI to changes in the instrument's throughput may be exploited to retrieve information about the degradation of the instrument, (2) to show that currently available methods to handle instrument degradation for SCIAMACHY are not accurate enough for the AAI because of its high sensitivity to (remaining) errors in the radiometric calibration, and (3) to introduce a new methodology to analyze and correct the Earth reflectance from satellite instruments that suffer from instrument degradation. This correction method is based on in-flight monitoring of global means of the Earth reflectance. The introduction of this new method is the main purpose of this paper.

[6] The paper starts with an introduction of the satellite instrument SCIAMACHY in section 2. This is followed in section 3 by an introduction of the AAI and a description of the SCIAMACHY AAI developed by us. In section 4 we introduce and study the global mean of the AAI, and explore its role as a monitoring tool for satellite instrument degradation. In section 5 we introduce the new method to correct for instrument degradation. This method corrects the measurements of Earth reflectance made by SCIAMACHY and is tested by applying it to the SCIAMACHY AAI retrieval. In section 6 we compare our correction method with two other approaches for instrument degradation correction. The paper ends with a summary and conclusion.

2. Description of SCIAMACHY

[7] SCIAMACHY is a remote sensing spectrometer that measures sunlight reflected by the Earth's atmosphere over the wavelength range 240–2380 nm, with a spectral resolution characterized by a full width at half maximum of 0.22–1.48 nm [*Bovensmann et al.*, 1999]. The instrument is part of the payload of the Envisat satellite, which was launched on 1 March 2002. The Envisat platform was put into a near-polar, Sun-synchronous orbit at an altitude of 800 km, with a local crossing time of the equator of 10:00 LT for the descending node and an orbital period of about 100 min. The SCIA-MACHY instrument is capable of performing measurements in either nadir or limb viewing mode. These two modes usually alternate and their collected data are stored in blocks, called "states." In this paper we will only make use of the nadir mode of the instrument. The size of a typical nadir state is approximately 960×490 km^2 (across track $\times$ along track). This area is scanned in the along-track direction by the forward movement of the satellite, and in the across-track direction via an internal mirror scanning back (eastward in 1 s) and forth (westward in 4 s) every 5 s. The size of the nadir satellite footprint is therefore determined directly by the integration time (IT). Typical sizes of the footprints

are 60×30 km^2 (for an IT of 0.25 s) and 120×30 km^2 (for an IT of 0.5 s).

[8] Once per day SCIAMACHY observes the Sun for the purpose of radiometric calibration. Changes in the instrument's throughput are monitored when the instrument is operating in one of its "light path monitoring" (LPM) modes. In these LPM modes sunlight is observed via internal light paths that are assumed to be representative for the actual internal light paths in the nadir or limb measurement mode. The time series of the recorded throughput describe how the individual light paths are degrading. Correction factors for instrument degradation, called m-factors, are derived from the LPM data based on the assumption that the Sun may be regarded as a stable light source. More information on the LPM measurements and the derived m-factor correction are given by *Bramstedt* [2008] and *Bramstedt et al.* [2009] (see also SCIAMACHY m-factors homepage: http://www.iup.uni-bremen.de/sciamachy/mfactors/).

[9] The scientific objective of SCIAMACHY is to perform global measurements of various trace gases in the troposphere and stratosphere. Retrieved trace gases include ozone, NO_2, CH_4, CO, CO_2, and a variety of other trace gases [*Bovensmann et al.*, 1999]. For certain trace gases the atmospheric profiles are retrieved using the limb scanning mode of the instrument. Additionally, SCIAMACHY monitors aerosol presence and retrieves cloud information such as cloud fraction, cloud pressure, cloud optical thickness, cloud droplet radius, and cloud phase index. An overview of all available scientific products from SCIA-MACHY, and their validation status, can be found at http://www.sciamachy.org/products/.

3. Absorbing Aerosol Index

3.1. Definition of Residue and AAI

[10] The Absorbing Aerosol Index (AAI) was introduced to provide information about the presence of UV-absorbing aerosols in the Earth's atmosphere. It was originally developed for the TOMS series of satellite instruments [*Herman et al.*, 1997]. The AAI is derived from another quantity, the residue, which, in this paper, is defined as

$$r = -100 \left\{ \log_{10} \left(\frac{R_\lambda}{R_{\lambda_0}} \right)^{\text{obs}} - \log_{10} \left(\frac{R_\lambda}{R_{\lambda_0}} \right)^{\text{Ray}} \right\}. \quad (1)$$

In equation (1), R_λ denotes the Earth's reflectance at the top of the atmosphere (TOA) at wavelength λ. The Earth's reflectance, in this paper, is defined as

$$R = \frac{\pi I}{\mu_0 E}, \quad (2)$$

where I is the radiance reflected by the Earth atmosphere (in W m^{-2} sr^{-1} nm^{-1}), E is the incident TOA solar irradiance perpendicular to the solar beam (in W m^{-2} nm^{-1}), and μ_0 is the cosine of the solar zenith angle θ_0.

[11] In equation (1), the superscript $^{\text{obs}}$ refers to reflectances which are measured by, in this case, SCIAMACHY, while the superscript $^{\text{Ray}}$ refers to modeled Rayleigh reflectances. These reflectances are calculated for cloud-free and aerosol-free atmospheres in which Rayleigh scattering, absorption by molecules, Lambertian surface reflection as

well as surface absorption takes place. For the wavelengths involved, the wavelengths λ and λ_0 must lie in the UV, and were set to 340 and 380 nm, respectively, for the SCIA-MACHY AAI product described in this paper.

[12] The Rayleigh atmosphere in the simulations is bounded below by a homogeneous Lambertian surface having a wavelength-independent surface albedo A_s. This surface albedo is not meant to represent the actual ground albedo. It is obtained from requiring that the simulated reflectance equals the measured reflectance at the wavelength $\lambda_0 = 380$ nm:

$$R^{obs}_{\lambda_0} = R^{Ray}_{\lambda_0}(A_s). \tag{3}$$

In the calculation of the residue, one assumes that the surface albedo A_s is wavelength independent in the wavelength interval $[\lambda, \lambda_0]$. This is a reasonable assumption for most surfaces, but there are also surfaces for which this assumption is not justified, such as for "bare soil" surfaces [*Kleipool et al.*, 2008]. Based on calculations we estimate that resulting errors for cloud-free pixels for this type of surface are on the order of 0.5 index points. Next, the surface albedo A_s is used to calculate R^{Ray}_λ. Equation (1) can now be reduced to

$$r = -100 \log_{10}\left(\frac{R^{obs}_\lambda}{R^{Ray}_\lambda}.\right). \tag{4}$$

The residue, as defined above, can be used to detect the presence of absorbing aerosols over land and sea surfaces, and even in the presence of clouds when the absorbing aerosol layer overlies the clouds. When a positive residue ($r > 0$) is found, absorbing aerosols are detected. Negative or zero residues on the other hand ($r \leq 0$), suggest an absence of absorbing aerosols. Recent publications [*Penning de Vries et al.*, 2009; *Penning de Vries and Wagner*, 2011] have shown that negative residues are related to the presence of clouds and/or scattering aerosols. For that reason, the AAI is defined as equal to the residue r where the residue is positive, and it is not defined where the residue is negative.

3.2. Residue Calculation/Algorithm Setup

[13] The algorithm we use is based on the technique described by *de Graaf et al.* [2005]. The first step in this algorithm involves finding the artificial surface albedo A_s using equation (3). Note that the simulated reflectances $R^{Ray}_{\lambda_0}$ are created by Rayleigh scattering atmospheres which are bounded below by Lambertian surfaces. Under this condition, it is possible to separate the contribution of the surface to the TOA reflectance from that of the atmosphere according to [*Chandrasekhar*, 1960]

$$R^{Ray}(\mu, \mu_0, \phi - \phi_0, A_s) = R^0(\mu, \mu_0, \phi - \phi_0) + \frac{A_s T(\mu, \mu_0)}{1 - A_s s^\star}. \tag{5}$$

The term R^0 is the so-called path reflectance, which is the atmospheric contribution to the reflectance, i.e., the situation of zero surface albedo. The second term is the contribution of a surface with an albedo A_s. The parameter T is the total atmospheric transmission for the given zenith angles, $s^\star$ is the spherical albedo of the atmosphere for illumination from below, μ is the cosine of the viewing zenith angle θ, and likewise, μ_0 is the cosine of the solar zenith angle θ_0 defined

earlier. The parameters ϕ and ϕ_0 are the azimuth angles of viewing and solar direction, respectively.

[14] Combining equations (3) and (5) at the reference wavelength $\lambda_0 = 380$ nm yields

$$A_s = \frac{R^{obs}_{\lambda_0} - R^0_{\lambda_0}}{T_{\lambda_0}(\mu, \mu_0) + s^\star_{\lambda_0}\left(R^{obs}_{\lambda_0} - R^0_{\lambda_0}\right)}. \tag{6}$$

In equation (6), $R^0_{\lambda_0}$ denotes the (simulated) path reflectance at wavelength λ_0, which is constructed using a set of look-up tables (LUTs). The path reflectance can be expanded in a Fourier series. In our case, with a Rayleigh atmosphere, this expansion is exact with only three terms in the azimuth angle difference $\phi - \phi_0$:

$$R^0 = a_0 + \sum_{i=1}^{2} 2a_i(\mu, \mu_0)\cos i(\phi - \phi_0). \tag{7}$$

The idea of the algorithm is that with LUTs of a_0, a_1, a_2, T, and $s^\star$, one can easily calculate $R^0_{\lambda_0}$, A_s, R^0_λ, R^{Ray}_λ, and finally, the residue and AAI. The advantage of the approach as described here is that both the azimuthal dependence and the dependence on surface albedo are treated analytically, and are therefore not part of the LUTs.

3.3. Reflectance Look-Up Tables

[15] The LUTs were created using the radiative transfer code DAK, which is short for "Doubling-Adding KNMI" [*de Haan et al.*, 1987; *Stammes*, 2001]. This vector radiative transfer model (RTM) can calculate the TOA reflectance taking polarization into account, and it can include absorption by various gases and Lambertian surface reflection. Next to ozone absorption, we also included O_2–O_2 absorption. We used DAK version 3.1, which accounts for pseudospherical atmospheres.

[16] The RTM calculations at the two wavelengths λ and λ_0 were performed for cloud-free conditions in a standard midlatitude summer (MLS) atmosphere [*Anderson et al.*, 1986], for 42×42 combinations of the zenith angles μ and μ_0, for 7 ozone column values Ω of 50, 200, 300, 350, 400, 500, and 650 Dobson units (DU, 2.69×10^{16} molecules cm^{-2}), and for 9 surface heights h_s ranging from 0 to 8 km in 1 km steps. The variation of the surface height was achieved by removing an appropriate number of layers from the bottom of the model atmosphere. Such a removal of layers affects the ozone columns to a (very small) degree, which was compensated for by scaling the entire ozone profile in such a way that the original ozone column value was retained.

[17] The LUTs for each of the two wavelengths contain the parameters a_0, a_1, a_2, T, and $s^\star$. The calculations in equations (6) and (7) require (linear) interpolation over the zenith angles μ and μ_0, surface height, and ozone column.

3.4. SCIAMACHY AAI Retrieval

[18] The SCIAMACHY AAI product that is discussed in this paper is a direct implementation of the algorithm described in sections 3.1–3.3. The level 1 data archive that was used was formed by reprocessed data of version 6.0x from 1 August 2002 to 31 December 2009 and by consolidated data of version 7.0x from 1 January 2010 to 30
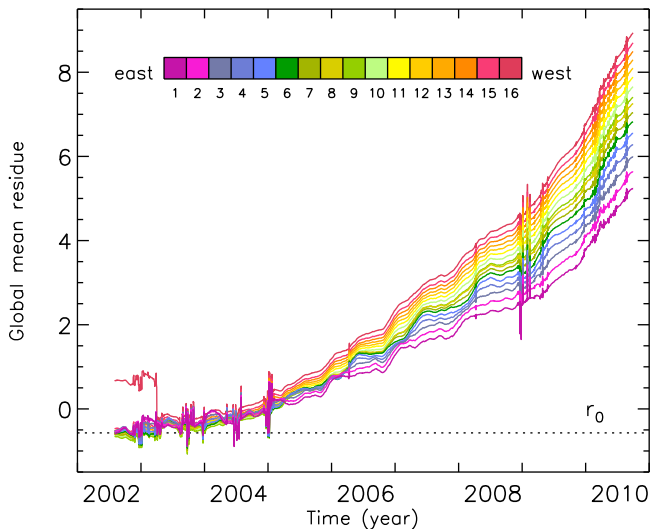
Figure 1. Time series of daily global mean residue calculated from SCIAMACHY observations as a function of time for the individual scan mirror positions. The colors indicate scan mirror positions, i.e., the position in the orbit swath. The time series cover the period from 1 August 2002 to 30 September 2010. The data were smoothed according to the procedure outlined in the main text. Notice the increase in the global mean residue with time and the growing scan angle dependence. No correction for instrument degradation was applied to the data.

September 2010. The reason for not using version 7.0x data for the entire time period is that the quality of version 7.0x level 1 data was affected by several processing problems that are still under investigation at the time of writing. The wavelength pair was set to $\lambda = 340$ nm, $\lambda_0 = 380$ nm and the respective SCIAMACHY TOA reflectances are averaged over one nm wide wavelength windows. The viewing and solar angles inside the SCIAMACHY level 1 product are given with respect to a height of 100 km above the Earth's surface. We perform a geometry correction to have these angles defined with respect to sea level, which is more representative for the actual situation. Surface height is calculated for each measurement footprint making use of an ETOPO-4 surface height database which was derived from the ETOPO-2 elevation database [*National Geophysical Data Center*, 2006]. Ozone column information is taken from the SCIAMACHY TOSOMI v0.43 ozone column product [*Eskes et al.*, 2005]. Back scan measurements are not processed and data with solar zenith angles greater than 85° are not used.

[19] Prior to the calculation of the residues, three types of corrections are applied to the Earth reflectances. First, we apply multiplicative time-independent correction factors $a_{340} = 1.008$ and $a_{380} = 0.989$ to account for radiometric calibration problems that are present from day one of the time series. These correction factors were determined on the basis of an approach described by *Tilstra et al.* [2005]. Second, for data until 31 March 2003 we apply multiplicative time-independent correction factors b_{340} and b_{380} to the reflectances of measurements performed at the westernmost position in the orbit swath [*Tilstra*, 2011]. This is to correct for an obstruction in the field of view (FOV) which affected

measurements at the western end of the orbit swath [*de Graaf and Stammes*, 2002]. The issue was solved on 31 March 2003 by shifting the orbit swath approximately 30 km to the east. Third, we correct the reflectances for instrument degradation, which is essential as shown in section 4. The approach we follow to determine the multiplicative time-dependent correction factors c_{340} and c_{380} is introduced in section 5.

[20] Sun glint flagging is an essential ingredient for the interpretation of the residues [*de Graaf and Stammes*, 2005] as specular reflection off the sea surface leads to anomalously high values for the retrieved residue. Flagging for Sun glint is done in the following way: the geometric condition for sun glint is checked, and if this condition is met, then a surface type database is consulted to determine if the footprint is located over sea. If this is the case, then we consider the residue possibly sun glint affected unless the scene is covered by a thick cloud cover. We consider a scene covered by a thick cloud when $c > 0.35$ and $p < 850$ hPa, where c is the scene's effective cloud fraction and p the cloud pressure. In this last step we make use of SCIAMACHY FRESCO v5.2 cloud information [*Wang et al.*, 2008]. Interference by solar eclipse events, which also results in too high residue values, is also flagged and the associated data are not used in this study. A more extensive discussion of the retrieval algorithm, settings, applied corrections, flagging and filtering is given in the Algorithm Theoretical Basis Document (ATBD) [*Tilstra*, 2011]. The SCIAMACHY AAI (and residue) data are available for download on the TEMIS Web site via the URL http://www.temis.nl/.

4. Monitoring Instrument Degradation

4.1. Daily Global Mean Residues

[21] In this section we will demonstrate that the AAI can be used as a sensitive indicator of changes in the radiometric response of a satellite instrument. To achieve this, we study time series of the daily global mean residue, which is defined as the mean of all residue measurements per day between latitudes 60°N and 60°S and with solar zenith angles θ_0 less than 85°. In Figure 1 we present the SCIAMACHY daily global mean residue as a function of time for each of the scan mirror positions that make up the orbit swath. The time series covers the period between 1 August 2002 and 30 September 2010, spanning more than 8 years. The integration time (IT) of the selected measurements was 0.25 s, resulting in 16 measurement footprints inside the forward scan of the instrument. Back scan measurements were not considered. The color bar in Figure 1 links the colors given to the time series to one of the 16 scan mirror positions, which also directly links them to a position in the orbit swath, as indicated.

[22] The SCIAMACHY global mean residue starts off relatively stable for all scan mirror positions and does so until the end of the year 2003, when it starts to increase rapidly, away from its initial mean value r_0. This initial value r_0 is represented in Figure 1 by the horizontal dotted line. At the end of the year 2004 a growing scan angle dependency sets in, making residues of the east and west side of the swath drift away from each other. At the end of the time series, in September 2010, the global mean residue has increased by more than 7 index points, stressing how
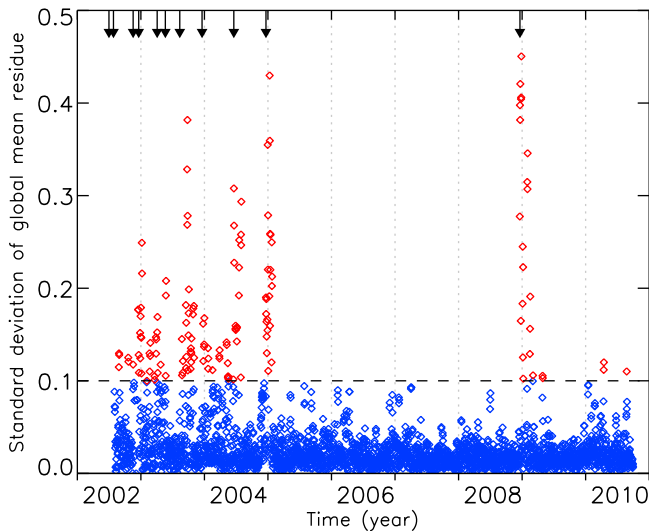
Figure 2. Day-to-day variation of the global mean residue, represented by the standard deviation of the daily global mean residues of days $n - 1$, n, and $n + 1$. The (long lasting) effects of instrument decontamination events, indicated by the arrows, on the radiometric calibration and the (global mean) residue are illustrated. The instrument was very stable in the period between the beginning of 2005 and the end of 2008, when no decontamination events were executed. For this period, the day-to-day variation in the global mean residue is generally below 0.05. Standard deviations above 0.1 are assumed to be caused by decontamination events and are plotted in red instead of blue.

sensitive residue and AAI are to changes in the absolute radiometric calibration of the measured Earth reflectances. At the same time, this sensitivity makes the AAI suited for monitoring instrument degradation.

[23] The time series for the westernmost scan mirror position initially shows significantly higher values compared to the time series for the other scan mirror positions. The higher values were caused by an obstruction of the FOV from inside the instrument, as explained in section 3.4. The results that are shown in the rest of the paper are obtained after application of the correction factors b_{340} and b_{380} to the reflectances of measurements performed at the westernmost position in the orbit swath. Also note the frequent outliers in the early years of the time series. These are related to scheduled instrument decontamination events, during which the onboard detectors were heated to get rid of ice and other forms of contamination. The impact on the residue remained noticeable up to a month after the various decontamination cycles had been completed.

[24] Smoothing was applied to the data shown in Figure 1 to somewhat better distinguish between the curves of different scan mirror positions. For the smoothing of the data we used the standard "central moving average" technique, removing neighboring outliers in the calculation of the averages. The moving averages were taken over 31 calendar days and outliers were identified on the basis of the standard deviations of adjacent days. The outliers themselves were not removed from the time series. To give an idea of the day-to-day variation in the global mean residue, we present in Figure 2 the nearest neighbor standard deviation of the

global mean residue, or more precisely, the standard deviation of the daily global mean residue created from the current, previous, and next day. Generally speaking, the standard deviation is below 0.05 index points. Exceptions can in almost all cases be traced back to instrument decontamination periods, or other known instrumental issues. Sudden injections of large amounts of aerosols in the atmosphere by regional events like dust storms do not seem to cause a noticeable day-to-day variation in the global mean residue. Thus, regional or local aerosol events do not contribute significantly to the day-to-day variation in the global mean residue.

4.2. Statistics and Temporal Variation

[25] The primary goal of this section is to show that the global mean residue can be considered to be more or less constant in time, despite the large seasonal variations that are found in regional or local aerosol presence. In Figure 3 we present two frequency distributions of the SCIAMACHY residue. The residues were calculated taking advantage of the in-flight reflectance degradation correction method introduced in section 5. The blue data points represent the residue histogram for the period November–December 2007 (ND). This period is characterized by relatively low global aerosol amounts. The red data points make up the histogram for the period covered by the 3 months July–August–September 2007 (JAS), representing the situation of relatively high
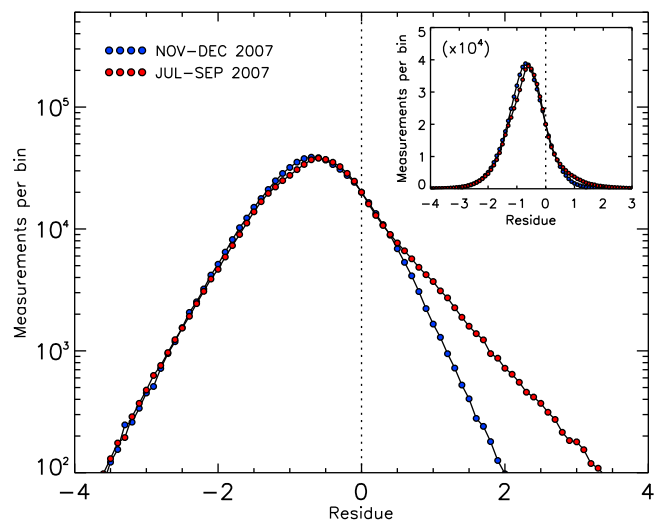

Figure 3. Frequency distributions of the residue, for November–December 2007 (ND, blue data points) and July–August–September 2007 (JAS, red data points). Instrument degradation was removed using the method introduced in section 5. The vertical scaling is logarithmic. The inset shows the same result but using linear scaling. Only observations relatively close to nadir view ($\theta < 11°$) were considered, to avoid a possible mixing of the underlying distributions for different viewing angles caused by geometry effects. In the months JAS the local and regional aerosol presence is known to be considerably higher than in the months ND. This is illustrated by the right tail of the histogram, which is clearly more populated in the months JAS. However, despite of this, the global mean residue is only slightly higher, to be precise: −0.58 (JAS) versus −0.69 (ND).

global aerosol amounts. Only measurements within the latitude band ranging from 60°N to 60°S were used, and only if their solar zenith angle θ_0 was below 80°. Sun glint situations were filtered out, as well as data affected by a solar eclipse. Moreover, only observations for which $\theta < 11°$ were accepted, to prevent a possible broadening of the distribution by a too large variation in viewing geometries. Note that the residue is dependent on the scattering geometry (see, for instance, *de Graaf et al.* [2005]). Finally, the histogram for ND was scaled with a factor N_{JAS}/N_{ND}, where N_{JAS} and N_{ND} are the total number of measurements collected in the histograms.

[26] The scale in the vertical direction of Figure 3 is logarithmic. The inset in the right upper corner contains the same data, but presented using linear scaling. The histogram for the months JAS is clearly more populated in the right wing of the distribution than the ND case is. The more pronounced wing is the result of the much higher global aerosol concentrations in the JAS period, mainly due to an increase in Saharan desert dust storms and biomass burning events in Africa. Note that the right wing of the distribution is also driven by other statistics, which is evident in the logarithmic representation. For comparison, the left wing of the JAS distribution, governed by cloud containing scenes, shows exactly the same behavior, and statistics, as the ND distribution. The much higher aerosol concentrations in the months JAS have definitely changed the global frequency distribution of the residue. However, the global mean residue has not changed much, despite the obvious response to the increased aerosol presence. The global mean residue over ND was −0.69 and the global mean residue over JAS amounted to −0.58, only slightly higher. Given the relatively small response of the global mean residue on the large seasonal variation in regional aerosol presence we can conclude that the influence of a possible long-term trend in regional aerosol presence would have a small impact on the global mean residue.

[27] Seasonal variations in the global mean residue are also driven by seasonal variations in the scattering geometry [*de Graaf et al.*, 2005]. In the case of SCIAMACHY, the seasonal variation in scattering geometry is entirely due to the changing solar position. The effect can, however, be calculated to be smaller than 0.3 residue index points for SCIAMACHY, depending on viewing zenith angle. This upper limit is also found empirically from Figure 8 which is introduced in section 5.4. In section 4.1 it is already noted that day-to-day variations in the global mean residue are relatively small. We can therefore regard the global mean residue as a constant value. This enables a form of self-calibration in which we correct the measured residues such that the measured daily global mean residue equals its expected constant value r_0. In the most simple form this would mean subtracting the difference between measured and expected global mean residue in a postprocessing step. This would have to be done for each individual scan mirror position in the case of scan angle-dependent instrument degradation. In the remainder of this paper, we will refer to this correction method based on a constant global mean residue as the AAI self-calibration method.

[28] Note that this simple correction of shifting the residue level is consistent with a multiplicative correction c_λ performed on the reflectance R_λ^{obs}. This can be found directly from inspection of equation (4). The shift Δr is thus directly related to the correction factor c_λ according to

$$\Delta r = -100 \log_{10} c_\lambda. \tag{8}$$

In other words, the effect of instrument degradation is in this approach attributed to instrument degradation manifesting itself at the shortest wavelength λ only. This first-order approximation will only work within certain boundaries, up to the level that instrument degradation cannot be corrected with a simple shift. For SCIAMACHY, this point is reached after ∼4 years, as shown in section 6.

4.3. Radiometric Change, Residue, and AAI

[29] Equation (8) expresses the simple relationship that exists between the radiometric change c_λ (at wavelength λ of the wavelength pair) and the resulting change in residue Δr. The dependence of the residue on c_{λ_0} (at wavelength λ_0 of the wavelength pair), however, is far from trivial because of the nonlinearity involved in the calculation of the residue [*de Graaf et al.*, 2007, section 2.4, equations (8) and (9)]. It is therefore impossible to perform a unique conversion from residue change to change in radiometric calibration. As a rule of thumb, though, a one percent change in radiometric calibration can typically be linked to an average change in residue of about half an index point. Note that the impact of radiometric change on residue and AAI is very similar. For changes in the reflectance at wavelength λ, the result is the simple shift (independent on scene properties) given by equation (8), and therefore the impact on residue and AAI is identical. For changes in the reflectance at wavelength λ_0, the impact on AAI and residue is in principle scene dependent. However, the impact on the global means of residue and AAI was found to be almost the same.

4.4. The m-Factor Correction

[30] Since some time, an official correction for instrument degradation, called m-factor correction, is available to the users of SCIAMACHY data [*Bramstedt*, 2008; *Bramstedt et al.*, 2009]. This m-factor correction is applied to the provided level 1 data (radiance and irradiance) and is based on the light path monitoring (LPM) measurements that are taken routinely by the SCIAMACHY instrument. In the LPM measurement modes the instrument observes the Sun via several different light paths inside the instrument. Instrument degradation is retrieved by assuming that the Sun is a stable source, and correction factors are calculated as a function of wavelength and time, and stored in a correction database. To study the performance of the m-factor correction, we present in Figure 4 the global mean residue calculated as before, but now with the m-factor correction (v6.01) applied to the level 1 product. The effects of instrument degradation on the residue, and on its global mean, are reduced considerably, but the scan angle dependency is not removed. This was expected, as the m-factors are currently defined to be scan angle independent.

[31] Currently, however, efforts are ongoing within the SCIAMACHY Quality Working Group (SQWG) to provide improved, scan angle-dependent m-factors in the near future. Note that the curve of the global mean residue of the easternmost scan mirror position seems to be the most stable of the curves in Figure 4. This can be explained by the fact that
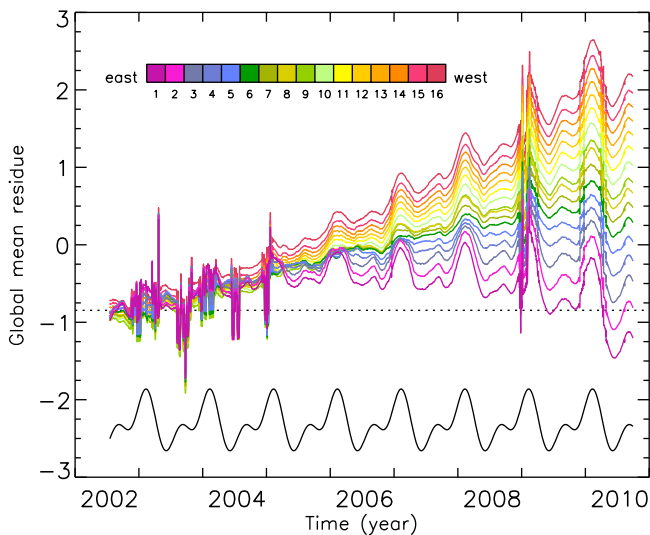
Figure 4. Time series of the daily global mean residue from SCIAMACHY, this time with the m-factor correction for instrument degradation (v6.01) applied to the level 1 product. In comparison to Figure 1, the effects of instrument degradation are reduced considerably, but the scan angle dependency is not removed. Also, periodic features, growing in strength with time, are introduced in the time series. These features are related to a seasonal variation in the elevation scan mirror position needed to be able to observe the Sun during calibration measurements. The black curve represents this position of the elevation scan mirror (in arbitrary units and without supporting vertical axis).

the correction factors were determined from a LPM measurement mode in which the position of the scan mirror coincides mostly with that of the easternmost viewing position. Unfortunately, apart from removing most of the effects of instrument degradation, the m-factors also introduce periodic features in the global mean residue. These are correlated with the seasonal variation in the position of the elevation scan mirror (ESM) needed to observe the Sun during LPM measurements when the Sun is observed via the instrument's subsolar port. The time dependence of the ESM angle in this mode is given in Figure 4 by the black curve. This curve was plotted using arbitrary scaling and is provided without vertical axis.

[32] What happens in the current (scan angle independent) m-factor calculation is the following. The seasonal variation in the ESM position that is used during subsolar LPM measurements, in combination with scan angle-dependent instrument degradation, leads to an artificial oscillation in the observed solar signal throughout the year which increases with time. This oscillation is, however, currently not attributed to the combination of scan angle-dependent instrument degradation and the variation in ESM position, but to pure scan angle-*independent* instrument degradation (the same for each scan mirror position). The m-factors intended for the correction of instrument degradation in the normal nadir radiance measurements are then correcting for an effect which was caused by a movement of the scan mirror, while the m-factors themselves are scan angle independent. The result is a fingerprint of the ESM mirror

variation in the nadir reflectance. This explains the periodic features in the derived global mean residue.

4.5. Conclusion

[33] The residue was shown to be very sensitive to changes in the radiometric response of SCIAMACHY. At the same time, the global mean residue should be more or less constant when calibration problems are absent. This makes the residue well suited for the monitoring of instrument degradation. It also allows a simple but robust form of self-calibration for the AAI product of a satellite instrument suffering from instrument degradation (discussed in section 4.2). This AAI self-calibration method will be accurate within about 0.4 index points. Many applications, such as analyses of long-term time series, require a higher degree of accuracy. To achieve such a higher level of accuracy, we introduce a more advanced method for the correction of instrument degradation in section 5.

5. In-Flight Reflectance Degradation Correction Method

[34] In this section we introduce a method to detect, analyze, and correct changes in the radiometric response of the SCIAMACHY instrument. The method is based on in-flight monitoring of global means of the reflectances that were measured. As the focus of this paper is on the SCIAMACHY AAI product, we will study global mean reflectances measured at 340 and 380 nm. However, the method is applicable to other wavelengths as well. Regional and zonal mean UV reflectances were presented by *Herman et al.* [2009] for other instruments and other time ranges.

5.1. Daily Global Mean Reflectances

[35] The global mean reflectance in this paper is defined as the mean of all SCIAMACHY reflectance measurements associated with latitudes between 60°N and 60°S and solar zenith angles θ_0 less than 85°. In contrast to the approach followed in section 4, sun glint situations are not filtered out. Since we want to study scan angle dependencies, we restrict ourselves to measurements performed with an IT of 0.25 s, which is the lowest possible IT for cluster 9 from which the 340 and 380 nm reflectances are retrieved. For this IT, there are 16 individual scan mirror positions making up the 4 s forward scan from east to west. We recorded all suitable reflectances from all days and orbits in the period between 1 August 2002 and 30 September 2010.

[36] The result for the 340 nm reflectance is shown in Figure 5. The gray curves represent the daily global mean reflectances for the 16 mentioned scan mirror positions, where the number $s = 1$ relates to the first and easternmost measurement of the forward scan (and to its associated scan mirror position), and the number $s = 16$ refers to the westernmost measurement in the forward scan. Back scan measurements, for which s would run from 17 to 20 (one back scan takes 1 s), were not considered. In order to be able to distinguish between the different reflectance time series, each time series was shifted vertically by + 0.05 with respect to the previous one, resulting in an offset of $(s - 1)0.05$.

[37] The gray data are showing a periodic time dependence on top of a downward trend, and relatively little noise. As for this noise, note that the SCIAMACHY instrument
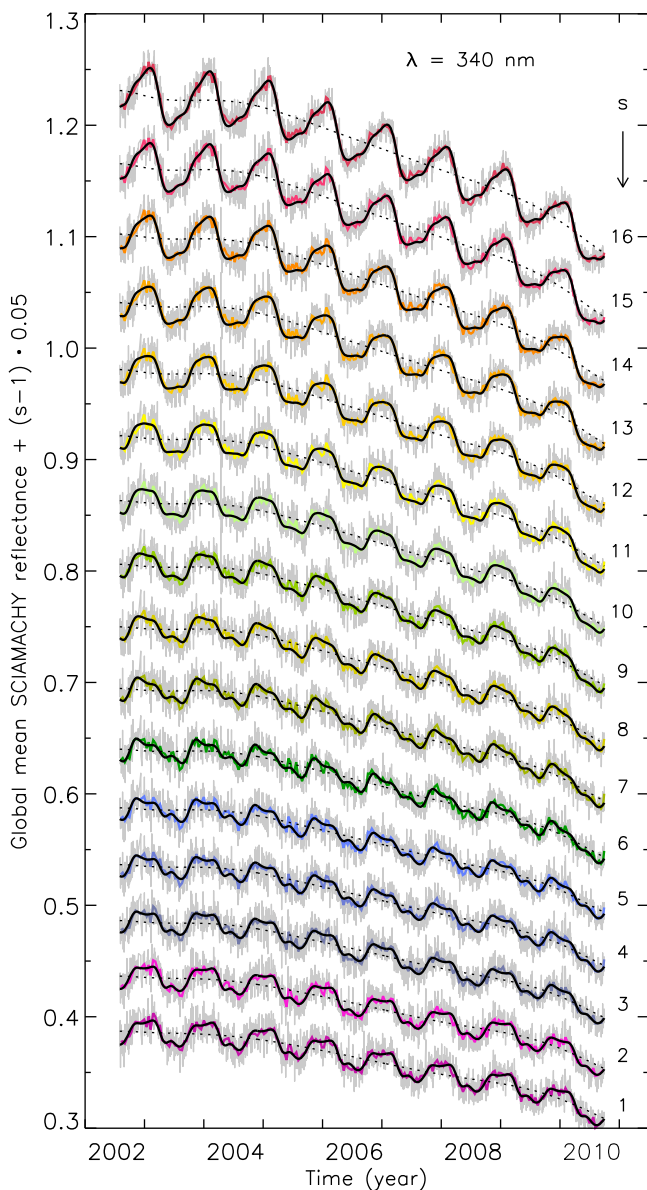
Figure 5. Global mean reflectance as defined in the text and measured at 340 nm by SCIAMACHY for each of its 16 (IT = 0.25 s) scan mirror positions. To separate the time series graphically, an offset of $(s-1)0.05$ was added to each, where s is the scan mirror position as indicated. The gray indicates the daily global mean reflectance, while the colored curves represent the 12 day average. Here the meaning of the colors is the same as in Figure 1. The solid and dotted black curves are described in the text: the dotted curve illustrates the effect of instrument degradation over the years.

only achieves global coverage in as much as 6 days. For that reason, we decided to average each 12 consecutive days. The colored time series in Figure 5 represent these 12 day averages, where the color usage is as in section 4. The fact that the colored data show such a stable periodic component suggests that it should be possible to accurately isolate and remove this seasonal variation from the time series, to obtain the reflectance change due to instrument degradation.

[38] To analyze the time series, we assume that the global mean reflectance, denoted by $R^{\star}$, may be well described empirically by a function made up of a polynomial term, representing the reflectance loss due to instrument degradation, multiplied by a term periodic in time that represents the seasonal variation of the global mean reflectance:

$$R^{\star}_{\lambda,s} = P^{(p)}_{\lambda,s}\left[1 + F^{(q)}_{\lambda,s}\right], \tag{9}$$

where the term $P^{(p)}_{\lambda,s}$ represents the polynomial part of degree p, defined by

$$P^{(p)}_{\lambda,s}(t) = \sum_{m=0}^{p} u^{(m)}_{\lambda,s} t^m, \tag{10}$$

while the seasonal variation $F^{(q)}_{\lambda,s}$ is described by a finite Fourier series of order q, according to

$$F^{(q)}_{\lambda,s}(t) = \sum_{n=1}^{q}\left[v^{(n)}_{\lambda,s}\cos(2\pi nt) + w^{(n)}_{\lambda,s}\sin(2\pi nt)\right]. \tag{11}$$

In equations (10) and (11), the parameter t is the time expressed in years since the beginning of the time series (1 August 2002). For the present study, we used $p = 10$ and $q = 5$. The resulting best fits for the 16 scan mirror positions are given in Figure 5 as solid black curves. The mean absolute deviation between fit and measurement is below 0.007 for all 16 time series. More relevant to this paper and the SCIAMACHY AAI product, however, are the dotted black curves, which represent the polynomial part $P^{(p)}_{\lambda,s}$ defined in equation (10). They represent the relative change in reflectance over the years, per scan mirror position, due to instrument degradation.

[39] Lower degrees of freedom in the fit functions, for instance for $p = 2$ and $q = 1$, would also lead to very acceptable and comparable fit results, especially for the polynomial part. The choice for $p = 10$ provides a lot of flexibility to fit the behavior of instrument degradation. This behavior is rather smooth for SCIAMACHY, but it may not be very smooth for other satellite instruments. The compact polynomial description of the reflectance loss allows a very simple and straightforward correction of the measured reflectances. At $\lambda = 340$ nm and 380 nm the correction for instrument degradation is

$$c_{\lambda,s}(t) = P^{(p)}_{\lambda,s}(0) / P^{(p)}_{\lambda,s}(t). \tag{12}$$

The reflectances at λ have to be multiplied with the correction factors c_{λ}. Polynomial coefficients describing the correction factors are listed in Table 1.

5.2. Reflectance Simulations

[40] The seasonal variations that were found in the global mean reflectances were assumed not to be caused by changes in radiometric response of SCIAMACHY nor by flaws in its radiometric calibration. To demonstrate that this assumption was indeed a justified one, we make use of radiative transfer calculations to simulate the seasonal variations that are shown in Figure 5. For our radiative transfer calculations we employ the same reflectance LUTs described in section 3.3 for the AAI. From these LUTs we

Table 1. Polynomial Coefficients $r_{\lambda,s}^{(m)}$ of the Correction Factor $c_{\lambda,s}$ for $\lambda = 340$ and 380 nm[a]

	340 nm							
	$m = 0$	$m = 1$	$m = 2$	$m = 3$	$m = 4$	$m = 5$	$m = 6$	$m = 7$
$s = 1$	1.00E+00	−6.98E−03	2.27E−02	−1.86E−02	7.95E−03	−1.62E−03	1.54E−04	−5.51E−06
$s = 2$	1.00E+00	−3.98E−03	1.73E−02	−1.51E−02	6.95E−03	−1.47E−03	1.43E−04	−5.18E−06
$s = 3$	1.00E+00	−4.06E−03	1.80E−02	−1.66E−02	7.87E−03	−1.69E−03	1.67E−04	−6.16E−06
$s = 4$	1.00E+00	−2.27E−03	1.45E−02	−1.46E−02	7.36E−03	−1.63E−03	1.64E−04	−6.12E−06
$s = 5$	1.00E+00	−2.94E−03	1.30E−02	−1.34E−02	7.05E−03	−1.60E−03	1.63E−04	−6.13E−06
$s = 6$	1.00E+00	5.15E−03	2.51E−04	−5.55E−03	4.65E−03	−1.20E−03	1.29E−04	−4.96E−06
$s = 7$	1.00E+00	7.10E−03	−2.00E−03	−4.38E−03	4.35E−03	−1.16E−03	1.26E−04	−4.87E−06
$s = 8$	1.00E+00	5.34E−03	1.31E−03	−6.69E−03	5.18E−03	−1.32E−03	1.41E−04	−5.43E−06
$s = 9$	1.00E+00	9.19E−03	−3.77E−03	−3.46E−03	4.12E−03	−1.13E−03	1.24E−04	−4.82E−06
$s = 10$	1.00E+00	1.32E−02	−1.06E−02	1.73E−03	2.19E−03	−7.55E−04	8.85E−05	−3.51E−06
$s = 11$	1.00E+00	2.42E−02	−2.67E−02	1.20E−02	−1.11E−03	−1.92E−04	3.98E−05	−1.84E−06
$s = 12$	1.00E+00	2.14E−02	−1.88E−02	4.92E−03	1.75E−03	−7.63E−04	9.50E−05	−3.90E−06
$s = 13$	1.00E+00	1.51E−02	−7.74E−03	−3.35E−03	4.80E−03	−1.34E−03	1.50E−04	−5.90E−06
$s = 14$	1.00E+00	1.02E−02	4.01E−03	−1.29E−02	8.35E−03	−2.01E−03	2.11E−04	−8.12E−06
$s = 15$	1.00E+00	1.88E−02	−3.93E−03	−1.00E−02	7.96E−03	−2.02E−03	2.16E−04	−8.43E−06
$s = 16$	1.00E+00	2.59E−02	−1.44E−03	−1.52E−02	1.03E−02	−2.48E−03	2.61E−04	−1.01E−05
	380 nm							
	$m = 0$	$m = 1$	$m = 2$	$m = 3$	$m = 4$	$m = 5$	$m = 6$	$m = 7$
$s = 1$	1.00E+00	1.63E−03	−2.93E−04	9.61E−04	1.18E−04	−7.80E−05	8.48E−06	−2.41E−07
$s = 2$	1.00E+00	−3.12E−03	5.08E−03	−2.39E−03	1.30E−03	−3.02E−04	2.95E−05	−1.01E−06
$s = 3$	1.00E+00	−3.50E−03	5.06E−03	−3.39E−03	2.07E−03	−5.06E−04	5.27E−05	−1.97E−06
$s = 4$	1.00E+00	−3.14E−03	4.19E−03	−3.24E−03	2.22E−03	−5.63E−04	6.02E−05	−2.31E−06
$s = 5$	1.00E+00	1.41E−03	−1.72E−03	−3.40E−05	1.37E−03	−4.46E−04	5.21E−05	−2.09E−06
$s = 6$	1.00E+00	9.34E−03	−1.40E−02	7.22E−03	−8.16E−04	−8.64E−05	2.16E−05	−1.04E−06
$s = 7$	1.00E+00	1.11E−02	−1.57E−02	7.88E−03	−9.45E−04	−7.29E−05	2.09E−05	−1.03E−06
$s = 8$	1.00E+00	9.51E−03	−1.29E−02	5.88E−03	−2.17E−04	−2.13E−04	3.44E−05	−1.54E−06
$s = 9$	1.00E+00	1.36E−02	−1.80E−02	9.02E−03	−1.24E−03	−3.22E−05	1.82E−05	−9.62E−07
$s = 10$	1.00E+00	1.67E−02	−2.36E−02	1.35E−02	−3.01E−03	3.25E−04	−1.68E−05	3.58E−07
$s = 11$	1.00E+00	2.88E−02	−4.17E−02	2.52E−02	−6.84E−03	9.87E−04	−7.47E−05	2.37E−06
$s = 12$	1.00E+00	2.71E−02	−3.55E−02	1.91E−02	−4.24E−03	4.51E−04	−2.18E−05	3.65E−07
$s = 13$	1.00E+00	1.99E−02	−2.34E−02	1.01E−02	−8.83E−04	−1.91E−04	3.88E−05	−1.86E−06
$s = 14$	1.00E+00	1.45E−02	−1.08E−02	−1.04E−04	2.91E−03	−9.03E−04	1.04E−04	−4.23E−06
$s = 15$	1.00E+00	2.48E−02	−2.06E−02	3.40E−03	2.44E−03	−9.11E−04	1.11E−04	−4.63E−06
$s = 16$	1.00E+00	3.27E−02	−1.79E−02	−2.21E−03	4.95E−03	−1.42E−03	1.60E−04	−6.41E−06

[a]The multiplicative correction factors $c_{\lambda,s}$ are calculated using the following expansion: $c_{\lambda,s}(t) = \sum_{m=0}^{7} r_{\lambda,s}^{(m)} t^m$.

can construct simulated reflectances for each of the individual SCIAMACHY measurements, with proper scattering geometry, surface height and ozone column, for any value of the (Lambertian) surface albedo.

[41] Clouds are not accounted for in the LUTs, but in the UV clouds behave fairly much as if they were Lambertian surfaces, at least, when their reflectivity is concerned [see, e.g., *Ahmad et al.*, 2004; *Koelemeijer and Stammes*, 1999]. The idea here is to treat the clouds as surfaces having a surface albedo equal to their effective cloud albedo A_c. To simplify matters, the cloud surfaces are modeled to lie on the Earth's surface. This simplification is allowed because the exact height of the cloud has a limited influence on the TOA reflectance in the UV [see, e.g., *Ahmad et al.*, 2004]. Scenes only partially covered by clouds are simply considered to be a mixture of clear-sky and fully clouded parts. This leads us to the following expression for the effective surface albedo $A_\star$ in the reflectance simulations:

$$A_\star = (1 - c)A_s + cA_c. \qquad (13)$$

Here c is the effective cloud fraction, and A_s and A_c refer to the surface albedo and cloud albedo, respectively. Equation (13) basically replaces equation (6) in section 3.2;

for the rest the calculation of the simulated reflectances is identical. The surface albedos $A_s(\lambda)$ and $A_s(\lambda_0)$ for each measurement were calculated using OMI-observed Lambertian equivalent reflectivity (LER) values [*Kleipool et al.*, 2008], while the effective cloud fraction c and cloud albedo A_c were obtained from the SCIAMACHY FRESCO cloud product [also see *Wang et al.*, 2008; http://www.temis.nl/fresco/]. The FRESCO algorithm uses the O_2-A band to retrieve cloud pressure and effective cloud fraction. The effective cloud fraction c is retrieved while keeping the cloud albedo A_c fixed to 0.8. Ozone column information and surface height were calculated in the same way as described in section 3.4. The model described above is admittedly simple, but in practice gives quite a good estimate for the TOA reflectance in the UV wavelength range.

[42] The resulting time series of the simulated global mean SCIAMACHY reflectance at 340 nm are given in Figure 6. As before, the gray curves denote daily global means and colored curves represent the 12 day average. The black curves are fits of $R_\lambda^\star = P_{\lambda,s}^{(p)}(1 + F_{\lambda,s}^{(q)})$ to the data, as before, but now with degrees of freedom $p = 0$ and $q = 5$. Comparing the graph with Figure 5, we see that the simulated time series follow the measured seasonal behavior in great detail. In fact, for the absolute values of the simulated
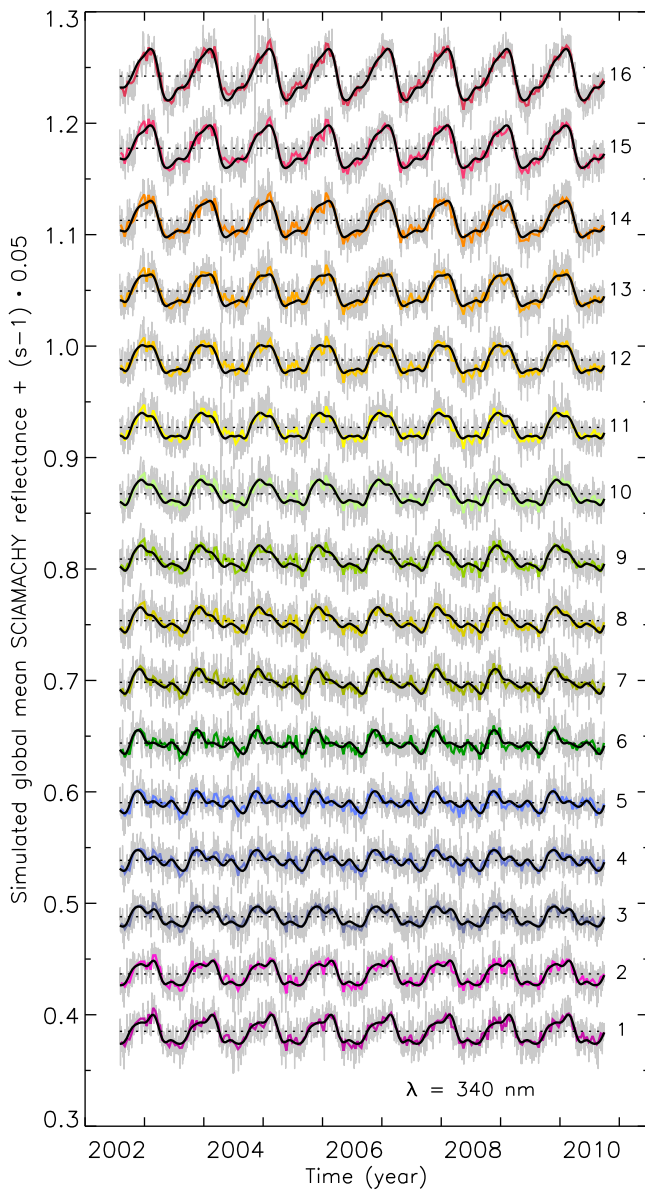
Figure 6. Simulated global mean SCIAMACHY reflectance at 340 nm versus time. The gray curves represent the daily global mean reflectance for each of the 16 SCIAMACHY scan mirror positions, while the colored curves represent the 12 day averages. The black curves are fit results of $R^{\star}_{\lambda,s} = P^{(0)}_{\lambda,s}(1 + F^{(5)}_{\lambda,s})$ as defined in section 5.1. The dotted curves represent the constants $P^{(0)}_{\lambda,s}$. The seasonal variations closely resemble the ones that were presented in Figure 5 for real data.

global mean reflectances we find a rather striking agreement with the measured global mean reflectances. However, the purpose of the reflectance simulations at this point is not to verify the absolute values of the global mean reflectance, but to explain the seasonal variations that were found in Figure 5. The simulation results presented in Figure 6 clearly show that the seasonal variations and their dependence on scan mirror position were indeed not caused by instrumental features or discrepancies in radiometric calibration, but by scene and/or geometrical variations.

5.3. Further Analyses/Radiometric Calibration

[43] Further analyses are needed to find out whether the seasonal variation in the global mean reflectance is caused by seasonal variations in the scattering geometry, or by seasonal variations in the degree of global cloud coverage. We start by applying the correction for instrument degradation introduced in section 5.1 to the SCIAMACHY reflectances. Then we apply a cloud filter to the data, based on (collocated) FRESCO cloud fractions. Next, we calculate the resulting daily global mean reflectances (covering the years 2002–2010), and distribute these over a complete calendar year made up of 7 day cells. After that, we take the mean value for each of these cells and analyze the result.

[44] In Figure 7 we present the seasonal variation of the global mean reflectance at 340 nm as a function of the day of the year, for the case without cloud filtering, given in the left window, and for the case with the cloud filter applied (only accepting $c < 0.05$), given in the right window. Like before, the time series were determined for each of the 16 scan mirror positions of SCIAMACHY, and an offset of $(s - 1)$ 0.05 was added to each of the time series, where the parameter s refers to the scan mirror position. Additionally, the black diamonds denote results obtained in the same way but using simulated reflectances based on the radiative transfer calculations that are described in section 5.2.

[45] Case 1, shown in Figure 7 (left), basically presents the same data as Figures 5 and 6, only the application of our correction for instrument degradation was added. Examining case 2 we see that the seasonal variations are very different from those of case 1. In particular, the seasonal variation at the eastern side of the swath ($s = 1$) was reduced considerably, but the seasonal variation at the western side of the swath ($s = 16$) is still rather strong. With the application of the cloud filter we removed most of the (seasonal) variation in the global cloud field, so the existence of a remaining seasonal variation in case 2 indicates that it is caused by a seasonal variation in the scattering geometry. At the same time, the seasonal variation was altered considerably by the applied cloud filtering. The conclusion must be that seasonal variations in both the scattering geometry and global cloud presence contribute to the seasonal variation found in the global mean reflectance.

[46] The absolute differences between the measured and simulated global mean reflectances for case 2 are within 0.002. The results shown in Figure 7 (right) therefore confirm the radiometric calibration correction factors a_{340} and a_{380} introduced in section 3.4. Remaining differences may be due to aerosols, non-Lambertian surface reflection, or sun glint. Sun glint is not included in the simulations.

5.4. Application to the SCIAMACHY AAI

[47] As an application of the in-flight reflectance calibration method, we apply the correction factors c_{340} and c_{380} defined in equation (12) to their associated reflectances before calculating the SCIAMACHY residues. To verify the reflectance calibration method, we study the effect of the applied reflectance correction by analyzing the resulting global mean residue in the way it was done in section 4. The result is shown in Figure 8. Figure 8 (top) shows the global mean residue for each of the scan mirror positions as a function of time. The effects of instrument degradation were
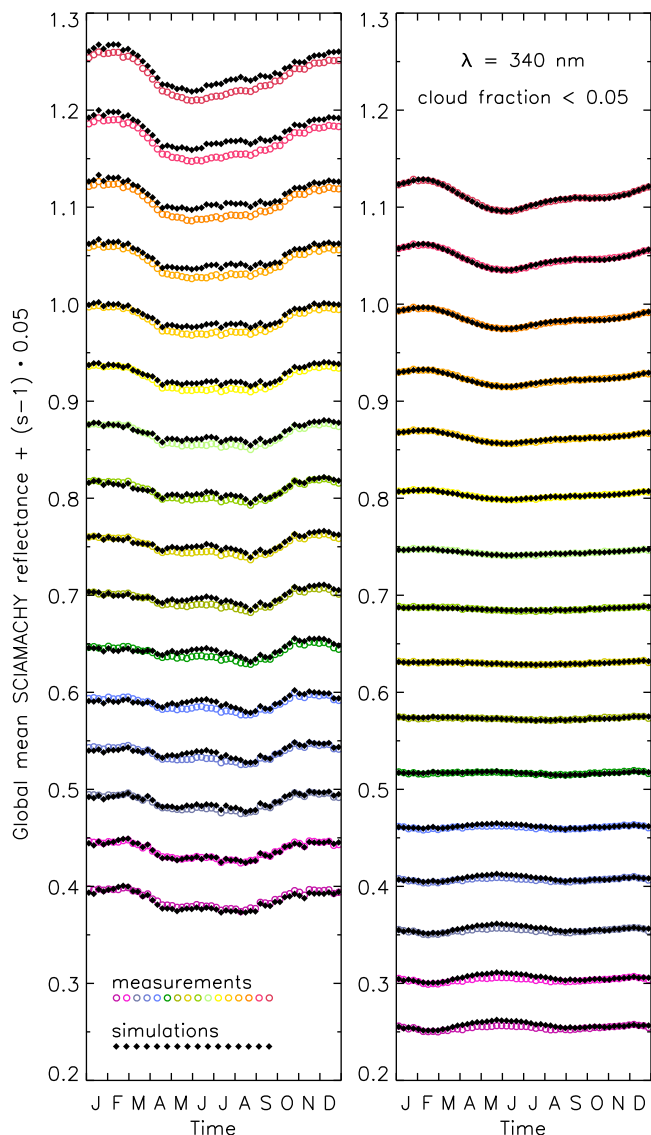
Figure 7. Seasonal variation of the global mean reflectance at 340 nm for all 16 SCIAMACHY scan mirror positions. An offset of $(s - 1)0.05$ was added to each of the time series, where s is the scan mirror position. The time series were given colors in line with Figure 1. (left) The situation where instrument degradation was removed using the method of section 5.1. (right) An additional cloud filter requiring that $c < 0.05$ was applied before determining the global means. The black diamonds denote simulation results of the global mean reflectance based on the radiative transfer calculations introduced in section 5.2.

indeed successfully removed. However, the outliers that were caused by various instrument decontamination events and occasional anomalies (see section 4) still exist, leading to rather high systematic errors of up to 0.5 index points for affected days. In Figure 8 (top) we indicate time periods in which (scheduled) decontamination events or known instrumental anomalies occurred using gray bars.

[48] In order to correct the residue data during the decontamination events we apply a multiplicative correction to the input reflectances R_λ and R_{λ_0} in such a way that the measured global mean reflectances $R_\lambda^\star$ and $R_{\lambda_0}^\star$ for each affected day are scaled to the global mean reflectances according to the fitted curves to $R_\lambda^\star$ (see Figure 5) and $R_{\lambda_0}^\star$ (not shown). Although this correction neglects the possibility of natural fluctuations in $R_\lambda^\star$ and $R_{\lambda_0}^\star$, it does set the important ratio of the reflectances R_λ and R_{λ_0} to a proper value. Note that this ratio is less susceptible to natural scene fluctuations than the parameters themselves. The corrections were applied and the resulting global mean residues were plotted in Figure 8 (bottom).

[49] The outliers have disappeared in almost all cases. The temporal behavior of the global mean residue time series is similar to that found for GOME-1 and GOME-2 [*Tilstra et al.*, 2010]. The AAI or residue data set used in the remainder of this paper is the one that was derived using the degradation correction described in this section; that is, it is the one that relates to Figure 8 (bottom).

6. Comparison of Correction Techniques

[50] Previously, we have discussed three different techniques to correct the retrieved SCIAMACHY AAI from the effects of instrument degradation: (1) the AAI self-calibration method described in section 4.2, (2) the m-factor correction described in section 4.4, and (3) our own reflectance correction method introduced in section 5.1/5.4. The methods 2 and 3 perform a correction on the reflectances. Method 1 in principle performs a correction on the residue, but this can be seen as a correction on the reflectance at 340 nm, as explained in section 4.2. We will first inspect and compare the global mean residues of the three methods. We will adopt method 3 as the reference method. The global mean residue for method 3 was
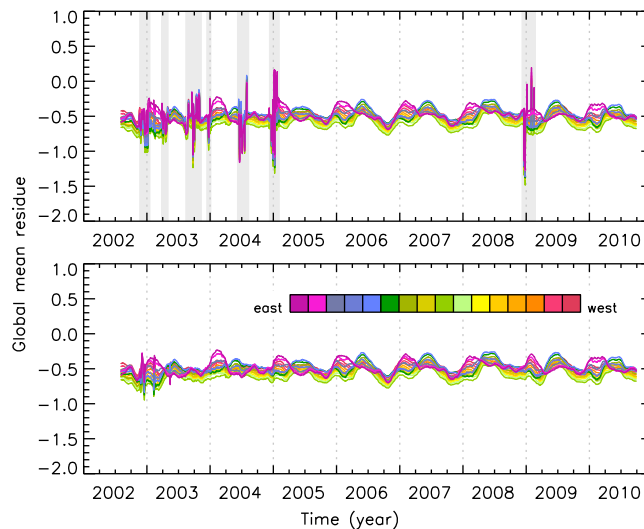

Figure 8. (top) Time series of the global mean SCIAMACHY residue per viewing direction after application of the reflectance correction for instrument degradation (as described in section 5.1). The trend caused by instrument degradation was successfully removed, but outliers related to instrument decontamination events still exist. Periods during which planned decontamination events or anomalies occurred are indicated by gray bars. (bottom) The outliers were removed by the method described in section 5.4.
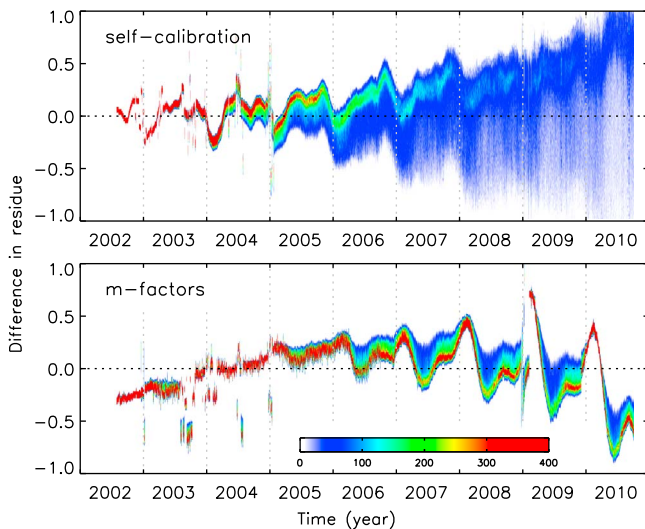
Figure 9. Time series of the distributions of residue differences. (top) The difference is that between the residues calculated using the degradation correction method introduced in section 5.1 and those calculated using the AAI self-calibration method discussed in section 4.2. (bottom) The difference is that between the residues calculated using the degradation correction method and the m-factor correction method described in section 4.4. The distributions were determined for each day, normalized, and the number of measurements per bin plotted using the color bar. The underlying residues were all taken from the easternmost part of the orbit swath to allow a fair comparison.

presented in Figure 8. Method 1 by definition fixes the global mean residue to a fixed value r_0. The small seasonal cycles in the global mean residue are ignored in this approach. The method may be improved by using a time-dependent, periodic r_0 that does include seasonal variations. Therefore, judging from the global mean residues alone, method 1 cannot be held inferior to method 3.

[51] As for method 2, the resulting global mean residue was given in Figure 4. The method is by construction scan angle independent, where methods 1 and 3 are not. As a result, the scan angle dependence of the global mean residue, caused by scan angle-dependent instrument degradation, is not removed. Apart from that, there is the growing periodic feature that affects the data. These problems were already discussed in section 4.4. The shortcomings are planned to be solved in the future. For a more fair comparison, we should focus on the easternmost scan mirror position, because this is the scan mirror position for which the (relevant) LPM measurements were performed (compare section 4.4). However, even when we do this, and when we ignore the aforementioned problems, there is an unrealistic upward trend for the early years of the time series which changes into a downward trend for later years. From inspection of the global mean residue we must therefore conclude that method 2 shows less promising results than methods 1 and 3.

[52] Because of the nonlinearity involved in equation (4), we cannot expect that the temporal behavior of the global mean residue completely describes the temporal behavior of all the underlying individual residues. In order to monitor

the differences between the three methods for *all* residue measurements, we determined the difference between residues according to method 1 or 2 and 3 for all individual measurements at the easternmost scan mirror position, for each measurement day. These differences were subsequently cast into histograms. This procedure was followed for all available measurement days. The time series of these histograms is visualized in Figure 9. Here the histograms are plotted on the vertical axis, where the colors used indicate the number of measurements for which the two data sets show a certain difference in residue. Figure 9 (top) shows the time series of histograms of the difference in residue between methods 1 and 3; Figure 9 (bottom) shows the same but for methods 2 and 3.

[53] The comparison between methods 1 and 3 in Figure 9 (top) shows that the residues according to method 1 follow those according to method 3 closely in the first 4 years. Only a small seasonal cycle is present, caused by the lack of seasonal variation in the global mean residue by method 1. In the later part of the time series, however, a spreading of the residue difference sets in. Method 1 differs from method 3 in that it effectively only holds the reflectance at 340 nm responsible for the effects of instrument degradation. The method basically assumes that only this reflectance needs to be tuned. It is this assumption that breaks down. The spreading gets quite severe at the end of the time series (up to two index points in magnitude).

[54] Figure 9 (bottom) presents the results based on the residue differences between methods 2 and 3. The spreading of the histograms again sets in at some point, but the effect remains limited throughout the entire time series. Outliers, caused by scheduled instrument decontamination events, are clearly visible. This is because the m-factors by definition do not try to correct data that were affected by these events. Note that the residue difference starts off at values around −0.3 instead of zero. This is caused by the application of the m-factors, which were found to introduce small corrections at $t = 0$. The limited spreading found in Figure 9 (bottom), as compared to in the upper window, is a direct consequence of the fact that the m-factor corrections on the wavelength pair for the eastern scan mirror position remain more or less in the correct range. If we focus on the westernmost scan mirror position instead of the easternmost scan mirror position, then the widening of the histograms is much larger. In fact, the widening goes up to one index points.

[55] From Figure 9 we conclude that a simple additive correction for instrument degradation applied to the residue will lead to large inaccuracies. For SCIAMACHY this point is reached after 4 years. Corrections should be applied to the reflectances at both wavelengths of the residue wavelength pair. The m-factor correction, in its current form, is also not able to provide a sufficient correction for instrument degradation. In early versions of our retrieval code we actually combined methods 1 and 2, hereby using method 1 as a postprocessing correction on the m-factor corrected residues (reflectances). This improved the results, but not to an accuracy within the 0.3 index point level, which we assume to be the minimal level of accuracy required for studies of time series of the AAI.

[56] In summary, we believe that the in-flight reflectance degradation correction method introduced in section 5.1 is needed to provide a reflectance correction with a high

enough accuracy to allow a proper determination of residue and AAI.

7. Summary and Conclusions

[57] The effects of instrument degradation on the AAI were studied using the scientific SCIAMACHY AAI product. From time series of the global mean residue we found that SCIAMACHY is suffering severely from scan angle-dependent instrument degradation and that (scheduled) instrument decontamination events have a large impact on the AAI. The AAI is very sensitive to instrument degradation: a one percent change in radiometric calibration can already result in a residue change of half an index point (compare equation (8)). At the same time, this makes the AAI very suited for analysis of instrument degradation: in the analyses we used the fact that the global mean residue should be more or less constant, and deviations were interpreted as signs of instrument degradation. The fact that the global mean residue shows a very limited time dependence was made plausible analyzing frequency distributions of the AAI.

[58] We also checked the official correction for instrument degradation, the so-called m-factor correction, which has been available to the SCIAMACHY user community since July 2007. We concluded that the m-factors correct most of the instrument degradation. However, the correction leaves quite a bit of room for improvement: (1) the correction is by definition scan angle independent, and the scan angle dependency that was found in the AAI is therefore not removed, (2) periodic features, growing with time, are introduced in the time series, and (3) even ignoring the two previous points of concern, the resulting AAI can be off by up to two index points. The m-factor correction may be satisfactory for most purposes but because of the AAI's high sensitivity to calibration errors the m-factor correction is not accurate enough.

[59] To cope with the problem of instrument degradation for the AAI a higher accuracy is therefore required. To this end, we introduced a new reflectance degradation correction method. This method is based on the analysis of time series of the global mean reflectance. In the case of SCIAMACHY, these time series show seasonal variations on top of a downward trend. In our analyses of the time series, the seasonal variations were described mathematically by a finite Fourier series fixed to a polynomial base which represents the change in reflectance response. The seasonal variations were removed as they do not represent instrumental artifacts. To be sure that this is indeed the case, we reproduced the seasonal variations in the global mean reflectance using simple radiative transfer calculations in which clouds are treated as Lambertian surfaces. The radiative transfer calculations also allowed us to study the origin of the seasonal variations. They are primarily caused by seasonal variations in scattering geometry and global cloud coverage.

[60] The reflectance correction factors were applied to the SCIAMACHY Earth reflectance and the derived AAI was examined by analyzing the global mean residue. All signs of instrument degradation had indeed been removed. Remaining were remnants of decontamination events. These could be removed as well with a small adjustment. To further analyze the behavior of our degradation correction method, we compared the derived AAI directly with the AAI based on the AAI self-calibration method and on the m-factor correction. The AAI self-calibration method does well, but only in the first years of instrument degradation. After that period, the correction fails. The AAI self-calibration method is therefore dismissed as a suitable correction. The m-factor correction also fails, mostly because of the problems mentioned at the beginning of this summary.

[61] In conclusion, in-flight degradation correction via the proposed new method can be done with a high accuracy. We estimate that the radiometric calibration errors due to instrument degradation can be brought back to within 0.2%. Note that the method in principle excludes the possibility of real geophysical trends in the Earth reflectance. However, the impact of a geophysical trend in the reflectance that exists over the studied time range, for instance, a trend in global cloud coverage, would be much smaller than the accuracy of the method. The goal of the method is to improve SCIAMACHY's calibration over the time period covered by its measurements. The method can be performed for each individual scan mirror position. Please note that the choice of applying the method to the UV (at 340 and 380 nm) was purely motivated by the decision to use the AAI as monitoring tool. We expect that the method of monitoring daily global mean reflectances would also work for shorter and longer wavelengths, provided that the noise due to instrumental and natural year-to-year variability is not exceedingly large. Finally, we would like to mention that the approach that was described in this paper was also applied successfully to GOME-1, and that the method may also be useful for application to GOME-2 on the Metop satellites.

References

Acarreta, J. R., and P. Stammes (2005), Calibration comparison between SCIAMACHY and MERIS onboard ENVISAT, *IEEE Geosci. Remote Sens. Lett.*, *2*(1), 31–35, doi:10.1109/LGRS.2004.838348.

Ahmad, Z., P. K. Bhartia, and N. Krotkov (2004), Spectral properties of backscattered UV radiation in cloudy atmospheres, *J. Geophys. Res.*, *109*, D01201, doi:10.1029/2003JD003395.

Anderson, G. P., S. A. Clough, F. X. Kneizys, J. H. Chetwynd, and E. P. Shettle (1986), AFGL atmospheric constituent profiles (0–120 km), *Rep. AFGL-TR-86-0110*, Air Force Geophys. Lab., Hanscom AFB, Mass.

Bovensmann, H., J. P. Burrows, M. Buchwitz, J. Frerick, S. Noël, V. V. Rozanov, K. V. Chance, and A. P. H. Goede (1999), SCIAMACHY: Mission objectives and measurement modes, *J. Atmos. Sci.*, *56*(2), 127–150.

Bramstedt, K. (2008), Calculation of SCIAMACHY m-factors, *Tech. Note IFE-SCIA-TN-2007-01-CalcMFactor*, Inst. of Environ. Phys., Univ. of Bremen, Bremen, Germany.

Bramstedt, K., S. Noël, H. Bovensmann, J. P. Burrows, C. Lerot, L. G. Tilstra, G. Lichtenberg, A. Dehn, and T. Fehr (2009), SCIAMACHY monitoring factors: Observation and end-to-end correction of instrument performance degradation, in *Proceedings of the 2009 Atmospheric Science Conference* [CD-ROM], edited by H. Sawaya-Lacoste, *Eur. Space Agency Spec. Publ.*, SP-676.

Burrows, J. P., et al. (1999), The Global Ozone Monitoring Experiment (GOME): Mission concept and first scientific results, *J. Atmos. Sci.*, *56*(2), 151–175.

Callies, J., E. Corpaccioli, M. Eisinger, A. Hahne, and A. Lefebvre (2000), GOME-2—Metop's second-generation sensor for operational ozone-monitoring, *ESA Bull.*, *102*, 28–36.

Chandrasekhar, S. (1960), *Radiative Transfer*, 393 pp., Dover, Mineola, N. Y.

de Graaf, M., and P. Stammes (2002), First verification of SCIAMACHY's absorbing aerosol index product, in *Proceedings of the Envisat Validation Workshop* [CD-ROM], edited by H. Sawaya-Lacoste, *Eur. Space Agency Spec. Publ.*, SP-531.

de Graaf, M., and P. Stammes (2005), SCIAMACHY Absorbing Aerosol Index—Calibration issues and global results from 2002–2004, *Atmos. Chem. Phys.*, 5, 2385–2394, doi:10.5194/acp-5-2385-2005.

de Graaf, M., P. Stammes, O. Torres, and R. B. A. Koelemeijer (2005), Absorbing Aerosol Index: Sensitivity analysis, application to GOME and comparison with TOMS, *J. Geophys. Res.*, 110, D01201, doi:10.1029/2004JD005178.

de Graaf, M., P. Stammes, and E. A. A. Aben (2007), Analysis of reflectance spectra of UV-absorbing aerosol scenes measured by SCIAMACHY, *J. Geophys. Res.*, 112, D02206, doi:10.1029/2006JD007249.

de Haan, J. F., P. B. Bosma, and J. W. Hovenier (1987), The adding method for multiple scattering calculations of polarized light, *Astron. Astrophys.*, 183, 371–391.

Eskes, H. J., R. J. van der A, E. J. Brinksma, J. P. Veefkind, J. F. de Haan, and P. J. M. Valks (2005), Retrieval and validation of ozone columns derived from measurements of SCIAMACHY on Envisat, *Atmos. Chem. Phys. Discuss.*, 5, 4429–4475, doi:10.5194/acpd-5-4429-2005.

Herman, J. R., P. K. Bhartia, O. Torres, C. Hsu, C. Seftor, and E. Celarier (1997), Global distributions of UV-absorbing aerosols from Nimbus 7/TOMS data, *J. Geophys. Res.*, 102(D14), 16,911–16,922, doi:10.1029/96JD03680.

Herman, J. R., G. Labow, N. C. Hsu, and D. Larko (2009), Changes in cloud and aerosol cover (1980–2006) from reflectivity time series using SeaWiFS, N7-TOMS, EP-TOMS, SBUV-2, and OMI radiance data, *J. Geophys. Res.*, 114, D01201, doi:10.1029/2007JD009508.

Jourdan, O., A. A. Kokhanovsky, and J. P. Burrows (2007), Calibration of SCIAMACHY using AATSR top-of-atmosphere reflectance over a hurricane, *IEEE Geosci. Remote Sens. Lett.*, 4(1), 8–12, doi:10.1109/LGRS.2006.881726.

Kleipool, Q. L., M. R. Dobber, J. F. de Haan, and P. F. Levelt (2008), Earth surface reflectance climatology from 3 years of OMI data, *J. Geophys. Res.*, 113, D18308, doi:10.1029/2008JD010290.

Koelemeijer, R. B. A., and P. Stammes (1999), Effects of clouds on ozone column retrieval from GOME UV measurements, *J. Geophys. Res.*, 104(D7), 8281–8294, doi:10.1029/1999JD900012.

Kokhanovsky, A. A., K. Bramstedt, W. von Hoyningen-Huene, and J. P. Burrows (2007), The intercomparison of top-of-atmosphere reflectivity measured by MERIS and SCIAMACHY in the spectral range of 443–865 nm, *IEEE Geosci. Remote Sens. Lett.*, 4(2), 293–296, doi:10.1109/LGRS.2007.894159.

Levelt, P. F., G. H. J. van den Oord, M. R. Dobber, A. Mälkki, H. Visser, J. de Vries, P. Stammes, J. O. V. Lundell, and H. Saari (2006), The Ozone Monitoring Instrument, *IEEE Trans. Geosci. Remote Sens.*, 44(5), 1093–1101, doi:10.1109/TGRS.2006.872333.

National Geophysical Data Center (2006), 2-minute gridded global relief data (ETOPO2v2), World Data Serv. for Geophys., U.S. Dep. of Commer., NOAA, Boulder, Colo. [Available at http://www.ngdc.noaa.gov/mgg/fliers/06mgg01.html.]

Noël, S., A. A. Kokhanovsky, O. Jourdan, K. Gerilowsky, K. Pfeilsticker, M. Weber, H. Bovensmann, and J. P. Burrows (2007a), SCIAMACHY reflectance and solar irradiance validation, in *Proceedings of the Third Workshop on the Atmospheric Validation of Envisat* [CD-ROM], edited by D. Danesy, *Eur. Space Agency Spec. Publ.*, SP-642.

Noël, S., K. Bramstedt, H. Bovensmann, J. P. Burrows, M. Gottwald, and E. Krieg (2007b), SCIAMACHY degradation monitoring results, in *Proceedings of the 2007 Envisat Symposium* [CD-ROM], edited by H. Lacoste and L. Ouwehand, *Eur. Space Agency Spec. Publ.*, SP-636.

Penning de Vries, M., and T. Wagner (2011), Modelled and measured effects of clouds on UV aerosol indices on a local, regional, and global scale, *Atmos. Chem. Phys.*, 11, 12,715–12,735, doi:10.5194/acp-11-12715-2011.

Penning de Vries, M. J. M., S. Beirle, and T. Wagner (2009), UV Aerosol Indices from SCIAMACHY: Introducing the Scattering Index (SCI), *Atmos. Chem. Phys.*, 9, 9555–9567, doi:10.5194/acp-9-9555-2009.

Stammes, P. (2001), Spectral radiance modelling in the UV-visible range, in *IRS 2000: Current Problems in Atmospheric Radiation*, edited by W. L. Smith and Y. M. Timofeyev, pp. 385–388, A. Deepak, Hampton, Va.

Tilstra, L. G. (2011), SCIAMACHY Absorbing Aerosol Index—Algorithm Theoretical Basis Document, *SRON Rep. SRON-EOS/RP/08-023*, R. Neth. Meteorol. Inst., De Bilt, Netherlands. [Available at http://www.temis.nl/airpollution/absaai/.]

Tilstra, L. G., and P. Stammes (2006), Intercomparison of reflectances observed by GOME and SCIAMACHY in the visible wavelength range, *Appl. Opt.*, 45(17), 4129–4135, doi:10.1364/AO.45.004129.

Tilstra, L. G., and P. Stammes (2007), Earth reflectance and polarization intercomparison between SCIAMACHY onboard Envisat and POLDER onboard ADEOS-2, *J. Geophys. Res.*, 112, D11304, doi:10.1029/2006JD007713.

Tilstra, L. G., G. van Soest, and P. Stammes (2005), Method for in-flight satellite calibration in the ultraviolet using radiative transfer calculations, with application to Scanning Imaging Absorption Spectrometer for Atmospheric Chartography (SCIAMACHY), *J. Geophys. Res.*, 110, D18311, doi:10.1029/2005JD005853.

Tilstra, L. G., O. N. E. Tuinder, and P. Stammes (2010), GOME-2 Absorbing Aerosol Index: statistical analysis, comparison to GOME-1 and impact of instrument degradation, paper presented at 2010 Meteorological Satellite Conference, Eur. Organ. for the Exploit. of Meteorol. Satell., Cordoba, Spain.

Torres, O., P. K. Bhartia, J. R. Herman, Z. Ahmad, and J. Gleason (1998), Derivation of aerosol properties from satellite measurements of backscattered ultraviolet radiation: Theoretical basis, *J. Geophys. Res.*, 103(D14), 17,099–17,110, doi:10.1029/98JD00900.

van Soest, G., L. G. Tilstra, and P. Stammes (2005), Large-scale validation of SCIAMACHY reflectance in the ultraviolet, *Atmos. Chem. Phys.*, 5, 2171–2180, doi:10.5194/acp-5-2171-2005.

von Hoyningen-Huene, W., A. A. Kokhanovsky, M. W. Wuttke, M. Buchwitz, S. Noël, K. Gerilowski, J. P. Burrows, B. Latter, R. Siddans, and B. J. Kerridge (2007), Validation of SCIAMACHY top-of-atmosphere reflectance for aerosol remote sensing using MERIS L1 data, *Atmos. Chem. Phys.*, 7, 97–106, doi:10.5194/acp-7-97-2007.

Wang, P., P. Stammes, R. van der A, G. Pinardi, and M. van Roozendael (2008), FRESCO+: An improved O_2 A-band cloud retrieval algorithm for tropospheric trace gas retrievals, *Atmos. Chem. Phys.*, 8, 6565–6576, doi:10.5194/acp-8-6565-2008.

I. Aben, Division of Earth and Planetary Science, SRON, Sorbonnelaan 2, NL-3584 CA Utrecht, Netherlands. (i.aben@sron.nl)

M. de Graaf, P. Stammes, and L. G. Tilstra, Climate Research and Seismology Department, KNMI, PO Box 201, NL-3730 AE De Bilt, Netherlands. (graafdem@knmi.nl; stammes@knmi.nl; tilstra@knmi.nl)